

Banner appropriate to article type will appear here in typeset article

# Interfacial dynamics induced by impacts across rigid and soft substrates

**Ishin Kikuchi<sup>1</sup>, Hiroya Watanabe<sup>1</sup>, Yuto Yokoyama<sup>2</sup>, Hiroaki Kusuno<sup>3</sup> and Yoshiyuki Tagawa<sup>4</sup>**

<sup>1</sup>Department of Mechanical Systems Engineering, Tokyo University of Agriculture and Technology, Tokyo 184-8588, Japan

<sup>2</sup>Micro/Bio/Nanofluidics Unit, Okinawa Institute of Science and Technology, Okinawa 904-0497, Japan

<sup>3</sup>Department of Mechanical Engineering, Kansai University, Osaka 564-8680, Japan

<sup>4</sup>Institute of Global Innovation Research, Tokyo University of Agriculture and Technology, Tokyo 184-8588, Japan

**Corresponding author:** Yoshiyuki Tagawa, [tagawayo@cc.tuat.ac.jp](mailto>tagawayo@cc.tuat.ac.jp)

(Received xx; revised xx; accepted xx)

---

We investigate impact-induced gas–liquid interfacial dynamics through experiments in which a liquid-filled container impacts substrates with elastic moduli from  $O(10^{-1})$  MPa to  $O(10^5)$  MPa. Upon impact, the concave gas–liquid interface inside the container deforms and emits a focused jet. When the jet velocity is normalized by the container impact velocity, all data collapse onto a single curve when plotted against the Cauchy number,  $Ca = \rho_e V_i^2 / E$ , which represents the ratio of the inertial force of the container–liquid system to the elastic restoring force of the substrate. The dimensionless jet velocity remains nearly constant for  $Ca < 10^{-4}$ , but decreases significantly for  $Ca > 10^{-4}$ . Based on this observation, we define the boundary between the *rigid-impact* and *soft-impact* regimes using the Cauchy number, providing a quantitative criterion for what constitutes “softness” in impact-driven interfacial flows. To explain the reduction in jet velocity observed in the *soft-impact* regime, we introduce a framework in which only the impulse transferred within the effective time window for jet formation contributes to interface acceleration. This concept, referred to as the *partial impulse*, captures the situation where the impact interval (the duration of contact between the container and the substrate) exceeds the focusing interval (the time required for jet formation). By modelling the contact force using an elastic foundation model and solving the resulting momentum equation over the finite impulse window, we quantitatively reproduce the experimental results. This *partial impulse* framework unifies the dynamics of impact-driven jetting across both rigid and soft substrate regimes, extending the applicability of classical impulse-based models.

**Key words:** Interfacial flows (free surface), Jets, Multiphase flow

## 1. Introduction

Impacts are relatively short-duration and violent phenomena involving solids or fluids that occur in a diverse range of situations. Familiar examples include wave impact on a seawall (Cooker & Peregrine 1995; Peregrine 2003), skipping stones on a water surface (Bocquet 2003; Rosellini *et al.* 2005; Tsai *et al.* 2022), and basilisk lizards running on water (Glasheen & McMahon 1996a,b; Hsieh & Lauder 2004). Engineering cases include violent wave impacts on ships, known as ship slamming (Kapsenberg 2011; Dias & Ghidaglia 2018), strong liquid impacts on container walls due to vibration, called liquid sloshing (Cooker & Peregrine 1995; Peregrine 2003), the entry of solid objects into liquid (Glasheen & McMahon 1996a; Thoroddsen *et al.* 2004; Grumstrup *et al.* 2007; Truscott *et al.* 2014; Rabbi *et al.* 2024), and the impact of a liquid drop on a solid surface (Cooker & Peregrine 1995; Josserand & Thoroddsen 2016; Philippi *et al.* 2016; Josserand *et al.* 2016; Philippi *et al.* 2018). When modelling phenomena involving such short-time dynamics, it is extremely effective to consider the impulse or the pressure impulse acting during the impact (Cooker & Peregrine 1995; Glasheen & McMahon 1996a,b; Peregrine 2003; Dias & Ghidaglia 2018; Philippi *et al.* 2018).

A common feature of impact problems is that they can be defined as the considerable acceleration of a boundary of the system over a short time (Philippi *et al.* 2018). One example of an impact problem that exhibits this feature is ‘Pokrovski’s experiment’ (Lavrentiev & Chabat 1980). This experiment is known for the formation of a focused liquid jet from the gas–liquid interface due to the rapid acceleration of the liquid caused by the impact (Milgram 1969; Antkowiak *et al.* 2007). The details of the formation process of this jet are as follows: when a liquid-filled test tube falls freely, the gas–liquid interface takes on a concave shape due to surface tension in the gravity-free reference frame. After the tube impacts a rigid substrate, the liquid is rapidly accelerated, and a focused jet is generated from the interface. In contrast, if the gas–liquid interface is flat just before impact, it does not deform after impact. The liquid simply rebounds together with the container from the substrate, and no jet is produced (Antkowiak *et al.* 2007).

Various studies have investigated Pokrovski’s experiment using rigid materials. Antkowiak *et al.* (2007) pointed out that the acoustic timescale of pressure wave propagation is much shorter than the impact duration, so liquid compressibility can be neglected. Therefore, the liquid motion during impact can be treated as an incompressible, momentum balance problem—much like a rigid-body impact—and the resulting pressure and velocity fields can be described using pressure–impulse theory. Kiyama *et al.* (2014) proposed a semi-empirical formula for the jet velocity based on pressure–impulse theory and the focusing effect of a concave gas–liquid interface (Tagawa *et al.* 2012; Peters *et al.* 2013). This formula accurately describes the jet velocity observed in Pokrovski’s experiment with a rigid substrate. Under stronger impacts, cavitation occurs inside the tube, which further increases the jet velocity (Kiyama *et al.* 2016). Watanabe *et al.* (2025) computed pressure–impulse fields by numerically solving the Laplace equation, using boundary conditions that prescribe the pressure impulse at the container bottom. They showed that the jet in Pokrovski’s experiment is driven by the pressure–impulse gradient. They also compared the numerically obtained pressure–impulse fields for containers with different convergence angles to analytical solutions from a reduced-order model. This comparison showed that the jet velocity is controlled by variations in the flow rate and by the pressure–impulse gradient along the centreline, both of which are influenced by changes in the container’s cross-sectional area. Onuki *et al.* (2018) improved Pokrovski’s experiment by inserting a capillary tube into the test tube so that the liquid level inside the capillary was lower than that outside. This level difference increased the pressure–impulse gradient in the capillary,

enabling the ejection of a highly viscous liquid with a kinematic viscosity of  $500 \text{ mm}^2/\text{s}$  or higher. They further pointed out that the jet formation process observed in Pokrovski's experiments can be understood as having two different timescales: the impact interval and the focusing interval. Onuki *et al.* (2018) defined the impact interval as the stage in which a pressure–impulse gradient generated by the impact rapidly accelerates the liquid, and the focusing interval as the stage in which the liquid is further accelerated by flow focusing at the concave gas–liquid interface after the impact. By applying high-viscosity jetting devices, impact-based coating systems for viscous liquids have also been developed. Kamamoto *et al.* (2021) succeeded in coating undiluted, highly viscous automotive paint, and Kobayashi *et al.* (2024) achieved continuous coating of silicone oil with a kinematic viscosity of  $500 \text{ mm}^2/\text{s}$  at a jetting frequency of 10 Hz. Other studies have also focused on jet formation in Pokrovski's experiment. Cheng *et al.* (2024) investigated the effect of viscosity on jet velocity, while Krishnan *et al.* (2022) examined the influence of the meniscus shape. Additionally, Krishnan *et al.* (2022) and Zhang *et al.* (2020) reported that rapid deceleration of the container can also generate a jet, highlighting that large accelerations applied to the container–liquid system are crucial for jet formation.

The insights from Pokrovski's experiment extend beyond jet formation. For example, Andrade *et al.* (2023) and Xie (2025) conducted experiments similar to Pokrovski's, using containers partially filled with swirling fluid, and reported that fluid dynamics can significantly reduce the rebound of such containers. They pointed out that the phenomenon can be explained by momentum transfer arising from water redistribution during impact. Additionally, Pan *et al.* (2017) focused on cavitation caused by rapid fluid acceleration and proposed a universal criterion to define its onset conditions.

The above reviews Pokrovski's experiment using rigid substrates, in which jet velocities were analysed mainly through pressure–impulse theory under the assumption of incompressibility. However, Pokrovski's experiment has also been conducted using soft substrates. Kurihara *et al.* (2025) varied the contact time between the container and the substrate from 0.11 ms to 2.2 ms by using metal, resin, and rubber substrates. They then investigated how the acceleration time of a liquid  $\Delta t$  affects the development of the pressure field within the liquid. They showed that pressure fluctuations in a liquid under rapid acceleration can be characterized by the Strouhal number ( $St = L/(c \Delta t)$ ), where  $L$  is the liquid filling height and  $c$  is the speed of sound), and that incompressible flow theory is applicable when  $St \leq 0.2$  (Kurihara *et al.* 2025). They also proposed a conceptual model that introduces a modified water-hammer theory accounting for the finite thickness of the pressure waveform. In a related study, Michele & Sammarco (2025) discussed the water-hammer phenomenon that occurs when a valve is operated slowly. They solved the nonlinear governing equations using a perturbation scheme combined with the Laplace transform, obtaining analytical solutions that show how the flow changes in space and time throughout the pipe. The study by Michele & Sammarco (2025) is closely related to that of Kurihara *et al.* (2025) in that it considers a finite liquid acceleration time by slowly operating a valve.

In the following, we organize the existing findings on Pokrovski's experiments and then present the objective of this study. In this study, the impact interval is redefined as the duration for which the container and the substrate remain in contact, while the focusing interval is redefined as the time required for a jet to form from a concave gas–liquid interface. Under this interpretation, the study by Kurihara *et al.* (2025) can be understood as elucidating the role of the liquid acceleration time in the formation of the pressure field during the impact interval. However, Kurihara *et al.* (2025) did not discuss the effect of a soft substrate on the focusing interval.

Here we extend Pokrovski's experiment to compliant substrates in order to isolate how substrate deformability alters the impulse used to deform the concave gas–liquid interface (hereafter denoted as  $I$ ) and, ultimately, the velocity of the focused jet. By varying the substrate elastic modulus over nearly six orders of magnitude (from  $8.1 \times 10^{-1}$  MPa to  $2.0 \times 10^5$  MPa), we lengthen the contact time from sub-milliseconds to 8 ms and access a regime in which the contact interval (i.e. the impact interval) overlaps with the jet-formation interval (i.e. the focusing interval). In this regime, the jet forms while the container is still in contact with the substrate, implying that the liquid interface cannot be driven by the fully transmitted impulse (i.e. the *total impulse*) assumed in conventional rigid substrate descriptions.

Our important result is that the dimensionless jet velocity collapses when plotted against the Cauchy number  $\rho_e V_i^2/E$ , and decreases markedly for  $\rho_e V_i^2/E > 10^{-4}$ . We interpret this decrease as a *partial impulse* effect: when the impact interval exceeds the focusing interval, only the impulse delivered within an effective time window set by the focusing dynamics contributes to jet acceleration. We formalize this idea by introducing an effective impulse window and combining it with an elastic foundation model, which together provide a quantitative description of jet velocities across both rigid and compliant substrates.

This paper is organized as follows. §2 describes the experimental setup and the data analysis. §3.1 presents the observed dependence of the jetting dynamics on the substrate stiffness. §3.2 shows that the data collapse when scaled by  $\rho_e V_i^2/E$  and identifies a compliant impact regime for  $\rho_e V_i^2/E > 10^{-4}$ , where the conventional rigid substrate picture fails. §3.3 develops the *partial impulse* framework and a predictive model, and compares the model with the experimental results. §4 summarizes the main conclusions.

## 2. Experimental setup

To investigate how a soft substrate affects the impulse  $I$  used to deform a concave gas–liquid interface, we conducted Pokrovski's experiment using nine substrates with different elastic moduli. Figure 1 shows the experimental setup. First, a test tube (Maruemu, A-16.5, inner diameter 14.3 mm, outer diameter 16.5 mm) was filled with silicone oil of  $10 \text{ mm}^2/\text{s}$  (Shin-Etsu Chemical, KF-96-10CS). Next, an aluminium plate with an iron S-shaped hook was attached to the top of the test tube using adhesive. The test tube was then placed on the substrate using an electromagnet (Fujita, round electromagnet FSGP-40). When the electromagnet was turned off, the test tube fell freely, and the gas–liquid interface was deformed by surface tension into a concave shape. After impact with the substrate, the interface deformed significantly, and a focused liquid jet was ejected. Two lights (HAYASHI-REPIC, LA-HDF158AA) were placed above the substrate to make it easier to observe the contact between the container and the substrate.

Table 1 summarizes the substrate material, elastic modulus  $E$ , size and thickness  $h$ , as well as the experimental conditions: the liquid filling height  $H$  and the impact velocity  $V_i$  of the impactor, which consisted of the test tube, the liquid, the aluminium plate and the S-shaped hook as a single unit. The experimental parameters were  $V_i$ ,  $H$  and  $E$ .  $V_i$  was varied from 0.63 m/s to 1.1 m/s by changing the drop height  $h_{\text{drop}}$  from 20 mm to 60 mm. Here,  $V_i$  was calculated using  $V_i = \sqrt{2gh_{\text{drop}}}$ , where  $g = 9.81 \text{ m/s}^2$  is the gravitational acceleration.  $H$  was used to change the mass of the impactor. For a rigid substrate, Kiyama *et al.* (2016) reported that the pressure–impulse gradient generated in the liquid at impact does not depend on  $H$ . Therefore, except when cavitation occurs, the jet velocity is independent of  $H$ . In contrast, in this study, we examine the effect of  $H$  on the jet velocity when  $E$  is small. For the metal substrate,  $H$  was set to 20 mm and 40 mm, while for the softer substrates with

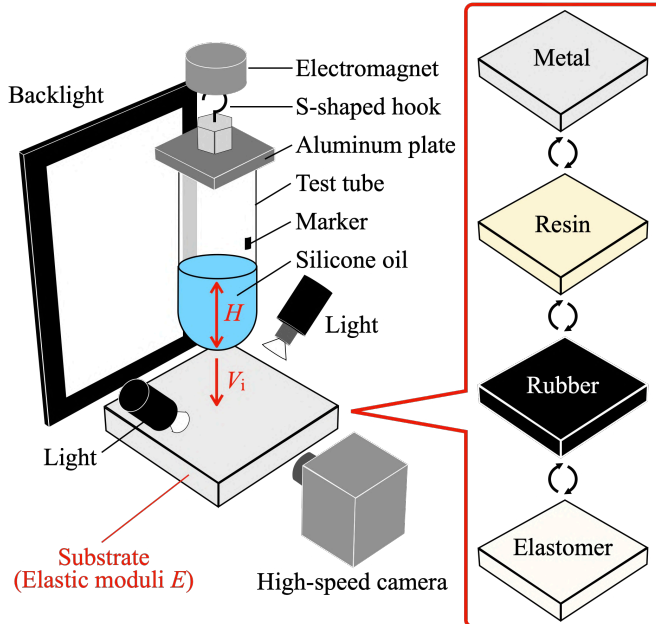


Figure 1. A schematic of the experimental setup. A test tube filled with silicone oil of  $10 \text{ mm}^2/\text{s}$  was released in free fall using an electromagnet to impact the substrate. The experimental parameters were the elastic moduli of the substrates  $E$ , the impact velocity of the impactor  $V_i$ , and the liquid filling height  $H$ . Nine substrates with different  $E$  made of metals, resins, rubber and elastomers were used.

lower elasticity,  $H$  was set to 20 mm, 40 mm and 60 mm. For all settings for  $H$ ,  $V_i$  and  $E$ , we checked the high-speed images to confirm whether cavitation occurred, and no cavitation larger than one pixel was observed. Therefore, we concluded that no cavitation contributing to jet acceleration, as reported by Kiyama *et al.* (2016), occurred in our experiments.  $E$  was varied from  $8.1 \times 10^{-1} \text{ MPa}$  to  $2.0 \times 10^5 \text{ MPa}$  by using nine types of substrates made of metal, resin, rubber and elastomer. For metal and resin substrates, the values of  $E$  were taken from the literature (Ashby & Jones 2012; Yahamed *et al.* 2016). The  $E$  values of the rubber and elastomer substrates were determined experimentally by pressing a rigid sphere against the substrate surface (Yokoyama *et al.* 2024). In this experiment, the load applied to the substrate was measured as a function of the imposed surface displacement.  $E$  was then obtained by applying an elastic foundation model that describes the relationship between the substrate displacement and the applied load (Johnson 1987) (see Appendix A). We fabricated the elastomer substrates using polydimethylsiloxane (PDMS) (see Appendix B). The elastic modulus of PDMS can be adjusted by changing the mass ratio of the base polymer (DOW, SILPOT 184 Silicone Elastomer Base) to the curing agent (DOW, SILPOT 184 Silicone Elastomer Curing Agent) (Shukla *et al.* 2016). We used three types of PDMS substrates with mass ratios of 10:1 (PDMS10), 20:1 (PDMS20) and 30:1 (PDMS30). To remove the stickiness of the PDMS substrate, baby powder (SiCCAROL-Hi, Asahi Group Foods Co., Ltd.) was applied to eliminate surface adhesion.

Images were captured using a high-speed camera (Photron, FASTCAM SA-X) with backlighting (PHLOX, White LED Backlight 400 × 200 mm). The frame rate of the camera was 10 000 fps, and the resolution was 0.160–0.169 mm/pixel. The images were used to analyse the jet velocity, the time at which contact between the container and the substrate ended ( $\tau_{\text{impact}}$ ), the time at which the centre of the interface rose due to flow focusing and the protrusion became visible from the side ( $\tau_{\text{focusing}}$ ), and the gas–liquid interface

Substrate	Material	$E$ [MPa]	Size [mm]	$h$ [mm]	$H$ [mm]	$V_i$ [m/s]
SS400	Steel	$2.0 \times 10^5$	150 × 150	20	20-40	0.63-1.1
A5052	Aluminium	$6.9 \times 10^4$	150 × 150	20	20-40	0.63-1.1
Epoxy	Epoxy resin	$3.0 \times 10^3$	150 × 150	20	20-60	0.63-1.1
ABS	Acrylonitrile Butadiene Styrene resin	$1.9 \times 10^3$	150 × 150	20	20-60	0.63-1.1
PE	Polyethylene resin	$7.0 \times 10^2$	150 × 150	20	20-60	0.63-1.1
Rubber	Rubber	$1.9 \times 10^1$	150 × 150	22.5	20-60	0.63-1.1
PDMS10	Polydimethylsiloxane	$5.7 \times 10^0$	100 × 100	22.0	20-60	0.63-1.1
PDMS20	Polydimethylsiloxane	$1.7 \times 10^0$	100 × 100	22.5	20-60	0.63-1.1
PDMS30	Polydimethylsiloxane	$8.1 \times 10^{-1}$	100 × 100	22.0	20-60	0.63-1.1

Table 1. A summary of the substrate materials, elastic moduli  $E$ , sizes, and thicknesses  $h$ , together with the values of the liquid filling height  $H$  and impactor impact velocity  $V_i$  for each substrate.

thickness  $H_m$  (as discussed in §3).  $\tau_{\text{focusing}}$  can be visually identified from the consecutive jet images in figure 4. The jet velocity was calculated from the relative position of the jet tip with respect to the test tube. The position of the test tube relative to the substrate was calculated using the printed marker on the test tube. For each experimental condition, the representative jet velocity  $V_j$  was defined as the jet velocity at  $t = \tau_{\text{focusing}}$  (see §3.1). From the high-speed camera images, it was confirmed that the concave shape of the gas–liquid interface just before impact, which strongly affects the motion of the gas–liquid interface (Antkowiak *et al.* 2007), did not change significantly across all conditions. The jet generation was repeated five times for each set of conditions.

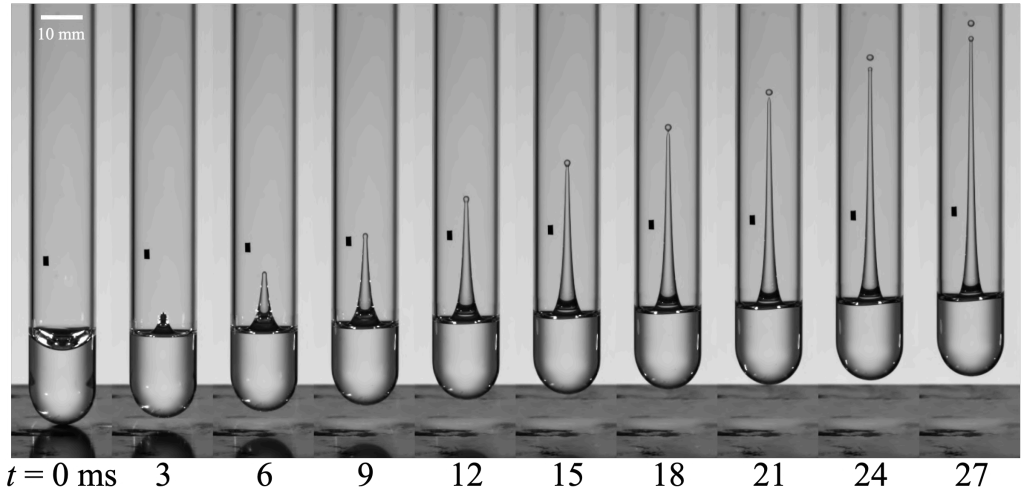
### 3. Results and discussion

In this section, §3.1 describes the typical interface motion and jet behaviour induced by impact onto substrates with various  $E$ . We also discuss the relationship between the substrate elasticity and the jet velocity. In §3.2, we show that the jet velocity can be described in a unified manner using the Cauchy number by organizing the experimental results through dimensional analysis. In §3.3, we clarify the mechanism of the reduced jet velocity on substrates with small  $E$  by discussing the impulse  $I$  used to deform a concave gas–liquid interface with proposing a concept of a *partial impulse*.

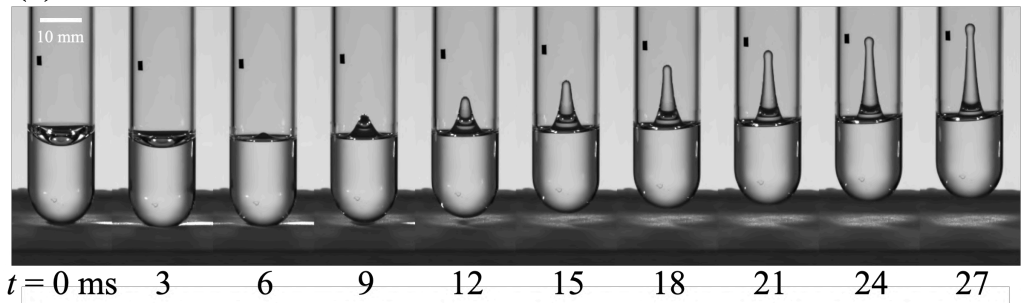
#### 3.1. Experimental observations of jet velocity reduction on soft substrates

In this section, we show that the jet velocity decreases as the substrate elasticity decreases. We also show that, for softer substrates, the time required to deform the concave gas–liquid interface clearly increases. Figures 2(a) and 2(b) show the interface motion and the jet behaviour for  $E = 2.0 \times 10^5$  MPa and  $E = 8.1 \times 10^{-1}$  MPa at  $H = 20$  mm and  $V_i = 0.63$  m/s. The time at which the container first makes contact with the substrate is defined as  $t = 0$  ms, and the time interval between each image is 3 ms. As mentioned in §2, when the electromagnet was turned off, the impactor fell freely and impacted the substrate. Following the impact, the flow was focused by the concave gas–liquid interface, leading to the ejection and elongation of a focused liquid jet. At  $t = 27$  ms, the jet tip was lower for  $E = 8.1 \times 10^{-1}$  MPa than for  $E = 2.0 \times 10^5$  MPa, which shows that the jet velocity was reduced. Furthermore, the time required for the concave interface to deform and generate a jet was longer for  $E = 8.1 \times 10^{-1}$  MPa than for  $E = 2.0 \times 10^5$  MPa. To quantify this difference, we investigated the time  $t = \tau_{\text{focusing}}$  when flow focusing was completed and the central part of the interface rose, making the protrusion visible from the side. At

(a)  $E = 2.0 \times 10^5$  MPa



(b)  $E = 8.1 \times 10^{-1}$  MPa



(c)

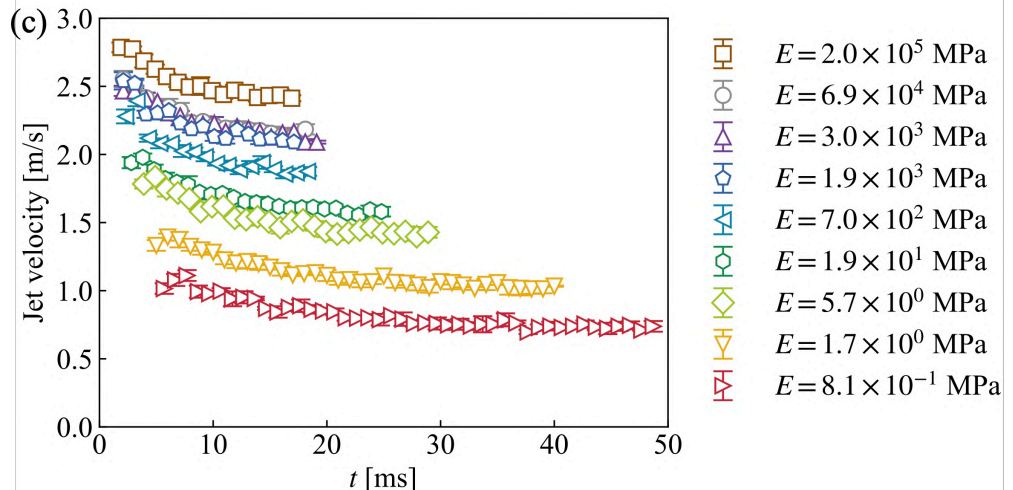


Figure 2. A comparison of the interface motion and jet behaviour for  $H = 20$  mm and  $V_i = 0.63$  m/s: (a)  $E = 2.0 \times 10^5$  MPa, (b)  $E = 8.1 \times 10^{-1}$  MPa.  $t = 0$  ms represents the time at which the container first makes contact with the substrate. For  $E = 8.1 \times 10^{-1}$  MPa, the time required for the concave interface to deform is longer, and the jet tip position is lower, compared with  $E = 2.0 \times 10^5$  MPa. (c) The time evolution of the jet velocity for different values of  $E$ . Here,  $t = 0$  ms represents the time at which the container first makes contact with the substrate; the plot starts at  $t = \tau_{\text{focusing}}$  and ends at the time of pinch-off. The results indicate that as  $E$  decreases, the jet velocity becomes slower, while  $\tau_{\text{focusing}}$  increases.

$E = 2.0 \times 10^5$  MPa,  $\tau_{\text{focusing}} = 1.9$  ms, while at  $E = 8.1 \times 10^{-1}$  MPa,  $\tau_{\text{focusing}} = 5.7$  ms, which is about three times longer.

Figure 2(c) shows the time evolution of the jet velocity in 1 ms intervals for each  $E$  at  $H = 20$  mm and  $V_i = 0.63$  m/s.  $t = 0$  ms denotes the time at which the container first makes contact with the substrate; the plot starts at  $t = \tau_{\text{focusing}}$  and ends at the time of pinch-off. Each plot represents the average of five trials, and the error bars indicate the standard deviation. It is clearly observed that the jet velocity decreases as  $E$  decreases. Looking at the starting points of the  $t = \tau_{\text{focusing}}$  plots for each  $E$ ,  $\tau_{\text{focusing}}$  increases with decreasing  $E$ . Moreover, the ending points of the plots also increase as  $E$  decreases, showing that the jet growth becomes slower. Focusing on the time evolution of the jet velocity, it reaches its maximum around  $t = \tau_{\text{focusing}}$  and then converges to a constant value. In the following sections, we use the representative jet velocity  $V_j$ , defined as the jet velocity at  $t = \tau_{\text{focusing}}$ .

Next, we discuss the relationship between  $V_j$  and  $E$ . Figure 3(a) shows the relationship between  $V_j$  and  $E$  for all experimental conditions on a semi-log plot. Each plot represents the average of five trials, and the error bars indicate the standard deviation. Overall,  $V_j$  tends to increase as  $E$  increases, but the data points do not collapse onto a single curve. In more detail, when  $V_i$  is fixed,  $V_j$  increases with increasing  $E$ , and when  $E$  is fixed,  $V_j$  increases with increasing  $V_i$ . These results show that  $V_j$  is strongly affected by both  $E$  and  $V_i$ . In the following sections, we derive a dimensionless number that can describe the relationship between  $V_j$  and  $E$  in a unified manner using dimensional analysis.

### 3.2. Jet velocity and Cauchy number: Dimensional analysis

In this section, we use dimensional analysis to show that the experimental jet velocities can be unified using the Cauchy number. We also show that for a Cauchy number smaller than approximately  $10^{-4}$ , the jet velocity can be described by the conventional pressure–impulse theory; this range is defined here as the *rigid-impact* regime. Furthermore, for a Cauchy number larger than approximately  $10^{-4}$ , the jet velocity decreases in a way that cannot be explained by conventional pressure–impulse theory. In this regime, the influence of the soft substrate on the interfacial motion becomes pronounced; therefore, we define this regime as the *soft-impact* regime.

We use dimensional analysis to derive a dimensionless number that collapses the relationship between  $V_j$  and  $E$ . Since the bottom of the impactor is hemispherical, the impact can be approximated as an impact between a rigid sphere and the substrate. We also assume that  $V_j$  can be expressed as a function of  $E$ ,  $V_i$ , and the effective density of the impactor,  $\rho_e$ , as

$$V_j \propto E^a V_i^b \rho_e^c. \quad (3.1)$$

Here,  $a$ ,  $b$ , and  $c$  are power exponents.  $\rho_e$  is calculated from the impactor mass  $m$  as follows:

$$\rho_e = \frac{3m}{4\pi R^3}, \quad (3.2)$$

which represents the density of a rigid sphere with the same outer diameter,  $2R$ , as the test tube, and varies with  $H$  in this experiment. Within the range of experimental conditions,  $H$  does not significantly affect  $V_j$  (see figure 3(a)). However, when a rigid sphere impacts a soft substrate, the sphere's density is one of the parameters that determines the type of contact, such as elastic or viscoelastic (Maruoka 2023). Because the contact force on the container from the substrate strongly depends on the contact type and affects the jet velocity, this study considers  $\rho_e$  as a parameter for  $V_j$ .

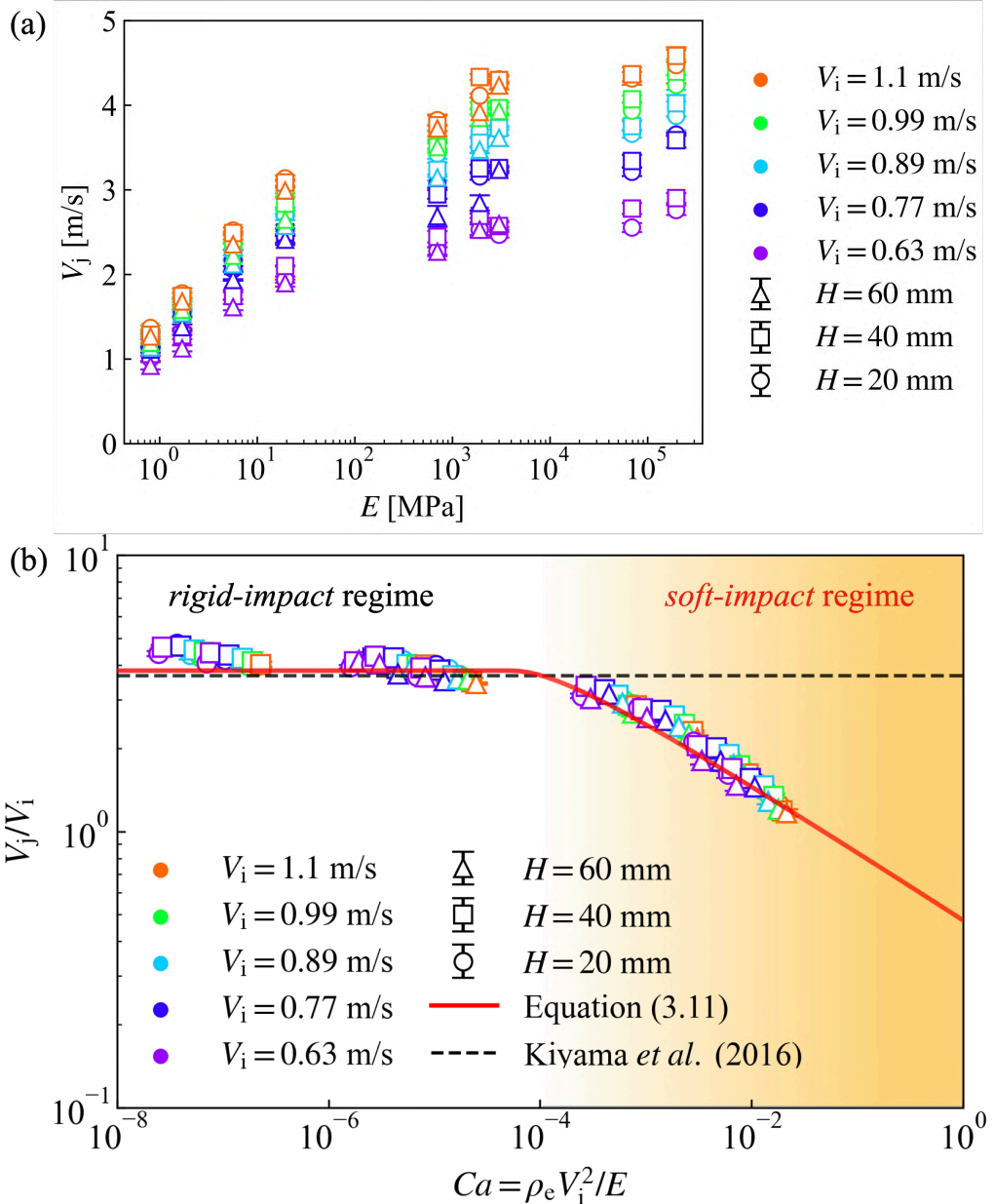


Figure 3. (a)  $V_j$  vs.  $E$ .  $V_j$  increases with increasing  $E$  at fixed  $V_i$  and also increases with  $V_i$  at fixed  $E$ , indicating that  $V_j$  strongly depends on both  $E$  and  $V_i$ . However, the data points do not collapse onto a single curve. (b)  $V_j/V_i$  vs.  $\rho_e V_i^2 / E$ . The black dashed line shows the  $V_j/V_i = 3.66$  estimated from the rigid substrate experiments by Kiyama *et al.* (2016), and the red line shows equation (3.11). All data collapse onto a single curve. When  $\rho_e V_i^2 / E < 10^{-4}$ , the variation in  $V_j/V_i$  is small. Since this regime can be explained by the pressure-impulse theory established in previous studies using rigid substrates, we refer to it as the *rigid-impact regime* in this paper. In contrast, when  $\rho_e V_i^2 / E > 10^{-4}$ ,  $V_j/V_i$  clearly decreases. This regime cannot be explained by conventional pressure-impulse theory. Because the influence of the soft substrate on the interfacial motion is pronounced, we refer to this region as the *soft-impact regime*.

Dimensional analysis gives

$$\frac{V_j}{V_i} \propto \left( \frac{\rho_e V_i^2}{E} \right)^{-a}, \quad (3.3)$$

where  $V_j/V_i$  represents the dimensionless jet velocity, obtained by normalizing  $V_j$  with  $V_i$ .  $\rho_e V_i^2/E$  is a dimensionless number known as the Cauchy number, which represents the ratio of the impactor's inertial force to the substrate's elastic force. The dimensional analysis shows that  $V_j/V_i$  can be scaled by the Cauchy number.

We next investigate the relationship between  $V_j/V_i$  and  $\rho_e V_i^2/E$  in detail using the experimental data. Figure 3(b) shows the dependence of  $V_j/V_i$  on  $\rho_e V_i^2/E$ . Each plot represents the average of five trials, and the error bars indicate the standard deviation. Compared with figure 3(a), all the plots in figure 3(b) collapse onto a single curve. A key feature of the relationship between  $V_j/V_i$  and  $\rho_e V_i^2/E$  is that around  $\rho_e V_i^2/E \sim 10^{-4}$ , the data separates into two regions: one where  $V_j/V_i$  changes little, and another where it clearly decreases.

In the region where  $\rho_e V_i^2/E < 10^{-4}$ , the value of  $V_j/V_i$  changes only slightly. This behaviour can be explained using the results of Kiyama *et al.* (2016), who reported the jet velocity in Pokrovski's experiment with metal substrates. Kiyama *et al.* (2016) reported that the dimensionless jet velocity  $V_j/U_0$ , where  $U_0$  is the velocity of the concave gas–liquid interface just after the impact, becomes  $V_j/U_0 = 2.05$  when cavitation does not occur. We estimate  $V_j/V_i$  from  $V_j/U_0 = 2.05$ , as reported by Kiyama *et al.* (2016), and compare it with our experimental data.  $U_0$  is defined as  $U_0 = V_i + V_r$ , where  $V_r$  is the rebound velocity of the impactor relative to the substrate (Kiyama *et al.* 2016). Because  $V_r$  can be estimated as  $V_r \approx eV_i$  using the restitution coefficient  $e$ ,  $U_0$  can be approximated by  $U_0 \approx V_i(1 + e)$ . Therefore, to estimate  $V_j/V_i$  from the value of  $V_j/U_0$  reported by Kiyama *et al.* (2016), we can use  $V_j/V_i \approx V_j(1 + e)/U_0$ .  $e$  was obtained by analysing  $V_r$  for the steel and aluminium substrates used in our experiments, and calculating  $e = V_r/V_i$  to give  $e = 0.787$ . We obtained  $V_r$  using the same method as Kiyama *et al.* (2016). We estimated  $V_j/V_i$  from  $V_j/U_0$  reported by Kiyama *et al.* (2016), and obtained  $V_j/V_i = 3.66$ . The black dashed line in figure 3(b) represents  $V_j/V_i = 3.66$ . We find that the result of Kiyama *et al.* (2016) captures the trend of  $V_j/V_i$  well in the region where  $\rho_e V_i^2/E < 10^{-4}$  in our experiments. This indicates that the jet velocity for  $\rho_e V_i^2/E < 10^{-4}$  can be explained by the theory established from Pokrovski's experiments using metal substrates. So far, the impact of a “fluid-containing container” on a rigid substrate has been modelled similarly to impacts between rigid bodies, using an incompressible-based approximation in which the *total impulse* from the substrate is transmitted almost instantaneously (Batchelor 1967; Antkowiak *et al.* 2007; Kiyama *et al.* 2014, 2016). The present results show that the applicability of this incompressible-based approximation can be evaluated using the Cauchy number. Furthermore, it is experimentally confirmed for the first time that the incompressible-based approximation is valid when  $\rho_e V_i^2/E < 10^{-4}$ . Therefore, in this study, the region  $\rho_e V_i^2/E < 10^{-4}$  is defined as the *rigid-impact* regime.

On the other hand, in the region where  $\rho_e V_i^2/E > 10^{-4}$ ,  $V_j/V_i$  decreases significantly with increasing Cauchy number. This region cannot be modelled using the incompressible-based approximation. In this study, we experimentally show for the first time that the effect of a small  $E$  becomes significant in fluid motion when  $\rho_e V_i^2/E > 10^{-4}$ . Therefore, we define the region  $\rho_e V_i^2/E > 10^{-4}$  as the *soft-impact* regime.

Since the *rigid-impact* regime and the *soft-impact* regime can be evaluated using the Cauchy number, these two regimes are determined not only by  $E$  but also by the contact

conditions, including  $V_i$  and  $\rho_e$ . However, under the present experimental conditions, the value of Cauchy number is predominantly determined by  $E$ . Therefore, the classification into the *rigid-impact* and *soft-impact* regimes can be readily made based on  $E$ . In the present experiments, all data for  $E \leq 1.9 \times 10^1$  MPa are classified into *soft-impact* regime, whereas all data for  $E \geq 7.0 \times 10^2$  MPa fall within *rigid-impact* regime. In the next section, we discuss the decrease of  $V_j/V_i$  in the *soft-impact* regime and clarify its underlying mechanism. Other studies have also used Cauchy number scaling to describe fluid motion with impact and the deformation of rigid bodies. For example, Hu & Li (2025) experimentally investigated the hydroelastic response of a vertical cantilever plate subjected to breaking-wave impacts. They showed that the plate deflection caused by the wave impact can be scaled by the Cauchy number, providing practical insights into hydroelastic effects under various impact conditions.

### 3.3. Mechanism of jet velocity reduction in the soft-impact regime

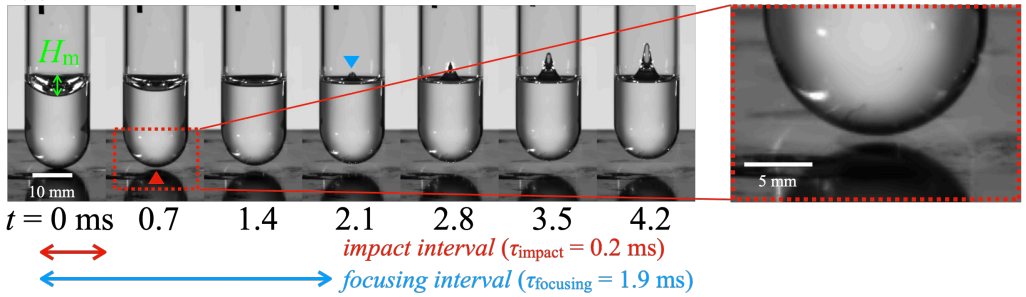
In this section, we elucidate the physical mechanism leading to the reduction of  $V_j/V_i$  observed for the *soft-impact* regime. The key observation is the relative ordering of two timescales: the impact interval  $\tau_{\text{impact}}$ , during which the container and substrate remain in contact, and the focusing interval  $\tau_{\text{focusing}}$ , required for the concave gas–liquid interface to focus and produce a visible jet. For rigid substrates,  $\tau_{\text{impact}} \ll \tau_{\text{focusing}}$ , so the contact force acts over a short interval, and the fluid subsequently focuses after the contact has ended. In this limit, it is natural to relate jetting to the *total impulse* delivered during contact.

For sufficiently soft substrates, however, we find  $\tau_{\text{impact}} > \tau_{\text{focusing}}$ , meaning that jetting starts while contact is ongoing. In that case, the interface cannot be driven by the *total impulse* transmitted over the entire contact, because the jet forms before that impulse has been fully delivered. This motivates a framework in which the jet is controlled by the impulse accumulated up to the jet-formation time, i.e., the *partial impulse*. Below we formalize this idea by (i) writing a momentum balance over the effective time window relevant for jet formation and (ii) modelling the contact force history using an elastic foundation model.

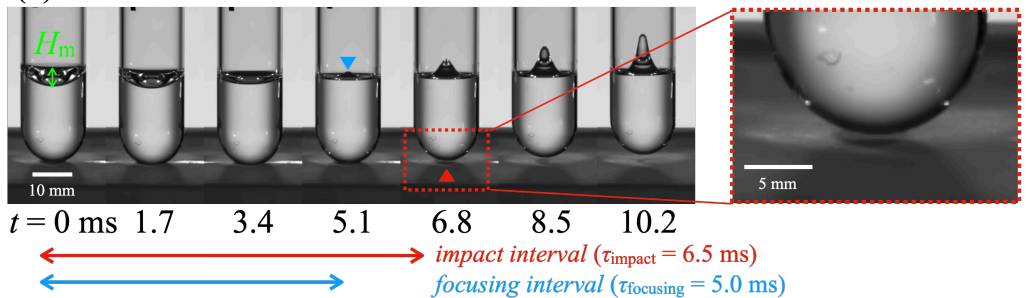
#### 3.3.1. Relative magnitude between the impact interval and the focusing interval

Figure 4 shows the moment when the container separates from the substrate (see  $\blacktriangle$ ) and the moment when the centre of the interface rises and a protrusion becomes visible from the side (see  $\blacktriangledown$ ) for  $H = 20$  mm and  $V_i = 0.63$  m/s. Panels (a), (b) and (c) correspond to  $E = 2.0 \times 10^5$  MPa,  $E = 1.7 \times 10^0$  MPa and  $E = 8.1 \times 10^{-1}$  MPa, respectively. The time  $t = 0$  ms denotes when the container begins to contact the substrate. The time when the container separates from the substrate is defined as  $t = \tau_{\text{impact}}$ . In this section,  $\tau_{\text{impact}}$  is interpreted as the time when the impact interval ends, and  $\tau_{\text{focusing}}$  as the time when the focusing interval ends. Here, we focus on the relative magnitudes of  $\tau_{\text{impact}}$  and  $\tau_{\text{focusing}}$ . In the *rigid-impact* regime, for  $E = 2.0 \times 10^5$  MPa,  $\tau_{\text{impact}} = 0.2$  ms and  $\tau_{\text{focusing}} = 1.9$  ms, giving  $\tau_{\text{impact}} \ll \tau_{\text{focusing}}$  (see figure 4(a)). This means that the impact interval is shorter than the focusing interval, and the jet forms while contact is still ongoing. In contrast, in the *soft-impact* regime, the order of  $\tau_{\text{impact}}$  and  $\tau_{\text{focusing}}$  is reversed. For  $E = 1.7 \times 10^0$  MPa,  $\tau_{\text{impact}} = 6.5$  ms and  $\tau_{\text{focusing}} = 5.0$  ms. For  $E = 8.1 \times 10^{-1}$  MPa,  $\tau_{\text{impact}} = 9.2$  ms and  $\tau_{\text{focusing}} = 5.7$  ms, and in both cases  $\tau_{\text{impact}} > \tau_{\text{focusing}}$ . This means that the impact interval is longer than the focusing interval, and the jet is formed during the contact (see figures 4(b, c)). The key point is that as  $E$  decreases, the relationship between  $\tau_{\text{impact}}$  and  $\tau_{\text{focusing}}$  is reversed, and the impact interval becomes longer than the focusing interval. This suggests

(a)  $E = 2.0 \times 10^5$  MPa



(b)  $E = 1.7 \times 10^0$  MPa



(c)  $E = 8.1 \times 10^{-1}$  MPa

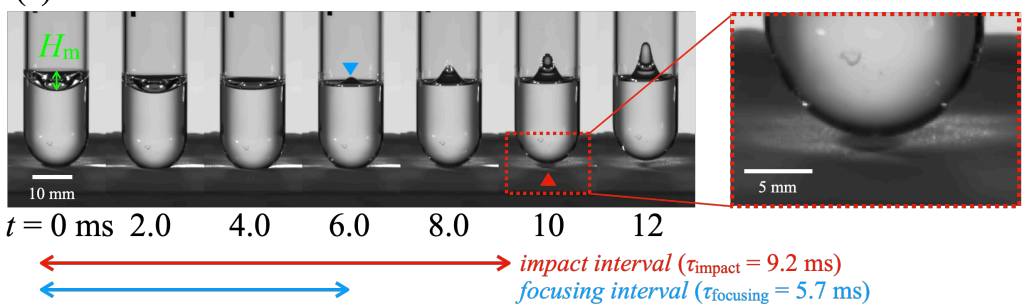


Figure 4. The moment when the container separates from the substrate (see  $\blacktriangle$ ) and when the centre of the interface rises and the protrusion becomes visible from the side (see  $\blacktriangledown$ ) are shown for (a)  $E = 2.0 \times 10^5$  MPa, (b)  $E = 1.7 \times 10^0$  MPa and (c)  $E = 8.1 \times 10^{-1}$  MPa ( $H = 20$  mm and  $V_i = 0.63$  m/s).  $t = 0$  ms denotes the time when the container begins to make contact with the substrate. For  $E = 2.0 \times 10^5$  MPa,  $\tau_{\text{impact}} = 0.2$  ms and  $\tau_{\text{focusing}} = 1.9$  ms, giving  $\tau_{\text{impact}} \ll \tau_{\text{focusing}}$ . In other words, the impact interval is short compared to the focusing interval. In contrast, for  $E = 1.7 \times 10^0$  MPa and  $E = 8.1 \times 10^{-1}$  MPa, the centre of the interface rises, and the protrusion becomes visible from the side while the container and the substrate are in contact. In other words, the impact interval becomes longer than the focusing interval.  $H_m$  represents the meniscus thickness just before the container and the substrate come into contact.

that, in the *soft-impact* regime, the *total impulse* from the substrate to the container is not fully transmitted to the concave gas–liquid interface before the jet is formed.

### 3.3.2. Development of a new model equation for the jet velocity

To discuss the mechanism behind the decrease in  $V_j/V_i$  on soft substrates, we model the jet velocity in terms of the impulse transmitted from the substrate during the time that is dynamically relevant for formation. In Pokrovski’s experiment, the impact generates a force on the container over a finite duration, which initiates the motion of the concave gas–liquid

interface and is subsequently amplified by flow focusing (Antkowiak *et al.* 2007; Kiyama *et al.* 2014). In the *rigid-impact* regime, the contact ends well before the jet forms, and it is therefore natural to relate the jet to the *total impulse* delivered during the contact. In the *soft-impact* regime, however, we observe  $\tau_{\text{impact}} > \tau_{\text{focusing}}$  (see figures 4), meaning that the jet forms while contact is still ongoing. In this case, the interface cannot be driven by the *total impulse* accumulated over the entire contact duration; instead, jet formation can only depend on the impulse delivered up to the end of the focusing interval.

This idea can be expressed without introducing additional variables by integrating the contact force over a finite time window. Importantly, this formulation automatically recovers the *rigid-impact* limit. When  $\tau_{\text{impact}} < \tau_{\text{focusing}}$ , the contact force vanishes for  $t > \tau_{\text{impact}}$ , and thus integrating up to  $t = \tau_{\text{focusing}}$  is equivalent to integrating over the full contact. In contrast, when  $\tau_{\text{impact}} > \tau_{\text{focusing}}$ , the upper limit  $t = \tau_{\text{focusing}}$  cuts off the force history, so that only a portion of the *total impulse* contributes to jet formation (see figure 5(b) and figures 6 (rigid-1) and (soft-1)–(soft-4)). In the remainder of this section, we translate this concept into a predictive model by combining momentum conservation with a contact-force model based on the elastic foundation model.

We consider the motion of the impactor of mass  $m$  over the interval from first contact,  $t = 0$ , to the end of the focusing interval,  $t = \tau_{\text{focusing}}$ . Figure 5(a) shows a schematic of the impactor and the substrate over the time interval  $[0, \tau_{\text{focusing}}]$ . Let  $F(t)$  denote the magnitude of the normal contact force exerted by the substrate on the container. Over  $[0, \tau_{\text{focusing}}]$ , momentum conservation gives

$$m(V_i + V') = \int_0^{\tau_{\text{focusing}}} F(t) dt. \quad (3.4)$$

Here,  $V'$  is the velocity of the impactor at  $t = \tau_{\text{focusing}}$ . Equation (3.4) therefore relates the impulse delivered up to  $t = \tau_{\text{focusing}}$  to the momentum change of the impactor over  $[0, \tau_{\text{focusing}}]$ .

Next, we relate the left-hand side of equation (3.4) to the jet velocity  $V_j$ . Based on pressure–impulse theory, Kiyama *et al.* (2014) related the change in momentum of the impactor to  $V_j$ . That is,  $V_j$  can be described by considering the change in momentum of the impactor over  $[0, \tau_{\text{focusing}}]$  as

$$V_j = \alpha(V_i + V'). \quad (3.5)$$

$\alpha$  is the strength of the flow-focusing effect after the interface acquires velocity due to the impact (Kiyama *et al.* 2016). The value of  $\alpha$  depends on the interface geometry (e.g. the contact angle at the wall) and on viscous effects (Kiyama *et al.* 2014; Cheng *et al.* 2024). In this study, the strength of the flow-focusing effect is calculated using the semi-empirical formula derived by Cheng *et al.* (2024) from experiments and simulations on rigid substrates. This semi-empirical formula accounts for the viscous boundary layer and is expressed as

$$\alpha = 2.05(1 - e^{-\zeta Re_p}). \quad (3.6)$$

$Re_p$  denotes the Reynolds number and can be written as

$$Re_p = \sqrt{\frac{RU_0}{\nu}}. \quad (3.7)$$

$U_0$  is the velocity of the concave gas–liquid interface just after the impact,  $\nu$  is the kinematic viscosity, and  $\zeta = 0.076$  is a fitting parameter (Cheng *et al.* 2024). For rigid substrates,  $U_0$  can be defined as  $U_0 = V_i + V_r$ , where  $V_r$  is the rebound velocity of the impactor (Kiyama

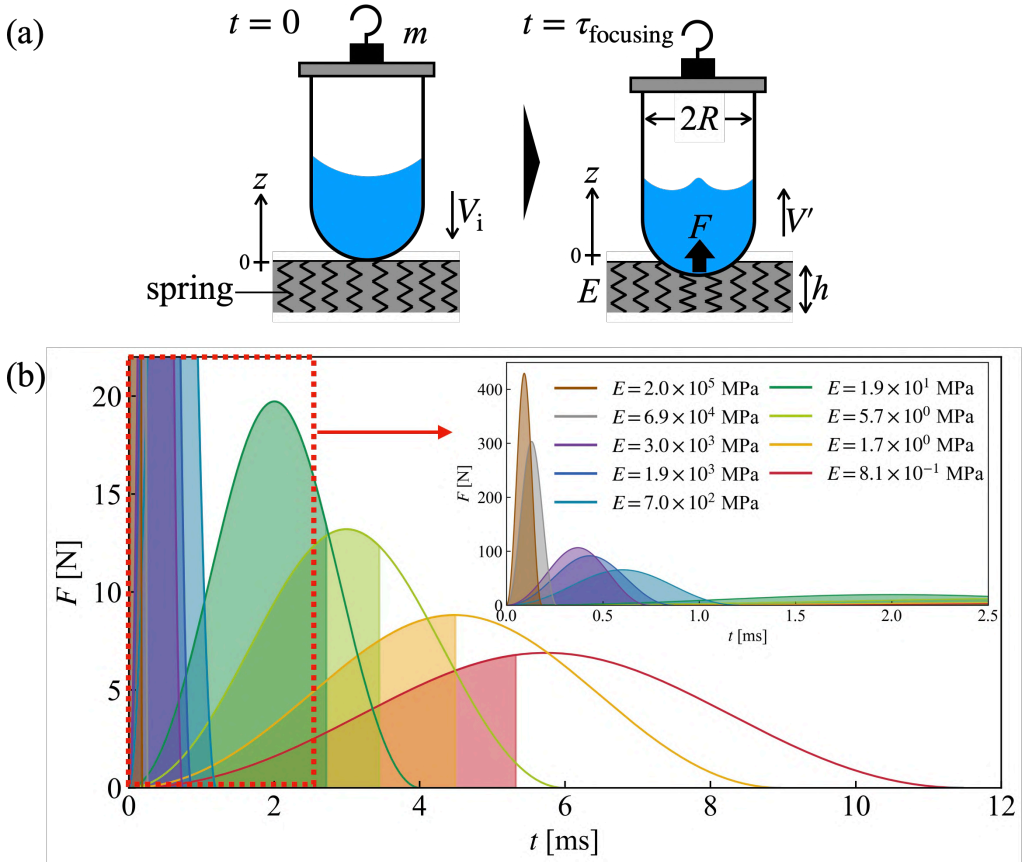


Figure 5. (a) A schematic of the impactor and substrate at  $t = 0$  and  $t = \tau_{\text{focusing}}$ .  $V'$  denotes the velocity of the impactor at  $t = \tau_{\text{focusing}}$ . In this study,  $F$  is evaluated using an elastic foundation model, in which the elastic response of the substrate is modelled as a spring. (b) The time evolution of  $F$  for each  $E$ , obtained from the elastic foundation model for  $H = 20$  mm and  $V_i = 0.63$  m/s. The shaded area represents  $I$  calculated from equation (3.11), i.e., the effective impulse time window. For  $E \geq 5.7 \times 10^0$  MPa, which falls within the rigid-impact regime, the jet is driven by  $I$  obtained by integrating  $F$  over its entire duration, i.e. the total impulse. In contrast, for  $E \leq 1.9 \times 10^1$  MPa, which belongs to the soft-impact regime, the jet is driven by the impulse  $I$  obtained from a partial integration of  $F$ , corresponding to a partial impulse.

et al. 2016, 2014; Cheng et al. 2024). We obtained  $U_0$  from the rigid substrate cases following the same procedure as in Kiyama et al. (2016, 2014) and Cheng et al. (2024), which yields  $\alpha = 1.91$  under the present experimental conditions. Equations (3.4)–(3.7) therefore relate the jet velocity to the time integral of the contact force over  $[0, \tau_{\text{focusing}}]$ .

We now model the right-hand side of equation (3.4). To describe the time history  $F(t)$ , we consider the one-dimensional contact dynamics of an impactor with a hemispherical bottom impacting a compliant substrate. Let  $z(t)$  denote the indentation of the substrate surface at the contact point (so that  $z = 0$  at first contact and  $z < 0$  during compression). Since the gravitational term is negligibly small compared with the other terms, the equation of motion is

$$m \frac{d^2 z}{dt^2} + F(z) = 0. \quad (3.8)$$

We apply the initial condition at  $t = 0$ ,  $dz/dt = -V_i$  and  $z = 0$ , to equation (3.8). The contact force  $F(z)$  can be theoretically obtained from the elastic foundation model using the displacement of the substrate surface (Johnson 1987), which is appropriate for finite-thickness substrates. For a rigid sphere (radius  $R$ ) indenting a substrate of thickness  $h$ , the model gives

$$F(z) = -\frac{\pi R E}{h} z^2. \quad (3.9)$$

The force model is validated through comparison with our measurements. The validity of the elastic foundation model for the present experiments is discussed in detail in Appendix C. As shown in figure 5(a), the elastic foundation model represents the substrate's elastic force using springs and describes the relationship between the contact force and the substrate surface displacement. The time variation of the contact force  $F(t)$  from the elastic foundation model can be obtained numerically using equations (3.8) and (3.9). First, by substituting equation (3.9) into equation (3.8), we obtain a nonlinear second-order ordinary differential equation (ODE) in  $z$  and  $t$ . We solve this ODE numerically using an explicit Runge–Kutta method (the `solve_ivp` function, an ODE solver from the SciPy library in Python) to obtain the time evolution of the substrate surface displacement  $z = z(t)$ . Finally, by substituting the numerically obtained  $z = z(t)$  into equation (3.9), we can calculate  $F(t)$ . As seen from equations (3.8) and (3.9),  $F(t)$  is determined by  $m$ ,  $h$ ,  $R$ ,  $V_i$  and  $E$ , but in the present experiments the most dominant parameter is  $E$ .

Figure 5(b) shows the time evolution of  $F$  for each  $E$  as solid lines for  $H = 20$  mm and  $V_i = 0.63$  m/s. The time when  $F$  becomes positive as the substrate, and the container begins to make contact, is defined as  $t = 0$  ms. The end of the solid line indicates the time  $t = \tau_{\text{impact}}$ , when  $F$  returns to zero as the substrate and the container separate. As  $E$  decreases, the peak of  $F$  decreases, while  $\tau_{\text{impact}}$  increases, consistent with softer contact.

Finally, we estimate  $\tau_{\text{focusing}}$  by assuming that a concave gas–liquid interface with a meniscus thickness  $H_m$  (see figure 4) deforms at a velocity  $V_j$ , as

$$\tau_{\text{focusing}} \approx \frac{H_m}{V_j}. \quad (3.10)$$

As shown in figure 4,  $H_m$  is defined as the distance between the upper and lower edges in the central region of the concave gas–liquid interface. By measuring the meniscus thickness just before impact for all experimental conditions, we obtained  $H_m = 5.41$  mm. Here,  $H_m$  can also be expressed using  $R$ . Using the contact angle  $\theta$  formed between the concave gas–liquid interface and the container wall and neglecting the wall thickness,  $H_m$  can be written geometrically as  $H_m = (R/\cos \theta)(1 - \sin \theta)$ .

By using equation (3.4)–(3.10), the impulse used to drive the concave gas–liquid interface  $I$  can be modelled. Therefore, a new closed model equation for the jet velocity can be written as

$$\frac{V_j}{V_i} = \frac{\alpha}{mV_i} \int_0^{\frac{H_m}{V_j}} F(t) dt. \quad (3.11)$$

Equation (3.11) reduces to the *rigid-impact* limit when  $H_m/V_j > \tau_{\text{impact}}$ , because the integral then covers the full force history. In the *soft-impact* regime, where  $H_m/V_j < \tau_{\text{impact}}$ , the upper limit  $t = H_m/V_j$  cuts off the integral, capturing the *partial impulse* mechanism proposed above. Based on the above considerations,  $I$  is formulated as the right-hand side of equation (3.11) as

$$I = \frac{\alpha}{mV_i} \int_0^{\frac{H_m}{V_j}} F(t) dt. \quad (3.12)$$

### 3.3.3. Numerical solution of the model equation

We further discuss  $I$  by numerically solving the model equation and comparing the results with the experimental data. First, we describe the numerical procedure used to solve equation (3.11). Since  $V_j$  appears on both sides of equation (3.11), the equation can be solved numerically by treating  $V_j$  as an unknown variable. Specifically, the integration time window of  $F$ , which is determined by the relative magnitudes of  $\tau_{\text{impact}}$  and  $H_m/V_j$ , is chosen such that the left-hand and right-hand sides of equation (3.11) are equal. This procedure yields the numerical solution for  $V_j$ .

First, we examine how the left-hand and right-hand sides of equation (3.11) vary as functions of an arbitrary  $V_j$ . Figure 6 shows how both sides of equation (3.11) depend on  $V_j$  for different values of  $E$  with  $H = 20$  mm and  $V_i = 0.63$  m/s. The  $x$ -axis represents an arbitrary  $V_j$ , while the  $y$ -axis shows  $V_j/V_i$  (line —) and  $I$  (lines —, — and —). The red, green and blue lines correspond to  $E = 8.1 \times 10^{-1}$  MPa,  $E = 5.7 \times 10^0$  MPa and  $E = 7.0 \times 10^2$  MPa, respectively. For each value of  $E$ , the numerical solution for  $V_j$  is given by the intersection of the black line (—) with the corresponding coloured line (—, — and —).

First, the value of  $V_j/V_i$  increases monotonically with a slope determined by  $V_i$ . In contrast, the behaviour of  $I$  varies depending on both the force profile  $F$ , which is primarily governed by  $E$ , and the integration time window, which is determined by the relative magnitudes of  $\tau_{\text{impact}}$  and  $H_m/V_j$ , as illustrated by (rigid-1) and (soft-1)–(soft-4) in figure 6. For  $E = 7.0 \times 10^2$  MPa, which falls within the *rigid-impact* regime,  $I$  remains constant. In contrast, for  $E = 5.7 \times 10^0$  MPa and  $E = 8.1 \times 10^{-1}$  MPa, both of which belong to the *soft-impact* regime,  $I$  exhibits a constant followed by a decreasing region.

First, we consider the case of  $E = 7.0 \times 10^2$  MPa. As shown in figure 6 (rigid-1), for  $V_j$  up to 5 m/s,  $H_m/V_j$  is larger than  $\tau_{\text{impact}}$ , and therefore the integration time window of  $F$  is  $[0, \tau_{\text{impact}}]$ . In this case,  $F$  is integrated over its entire duration. Because the integration time window does not depend on  $V_j$ , the value of  $I$  remains constant regardless of  $V_j$ . Figure 6 (rigid-1) shows the value of  $I$  at which  $V_j$  becomes the numerical solution for  $E = 7.0 \times 10^2$  MPa. When  $I$ , obtained by integrating the full force history, equals  $V_j/V_i$ , the corresponding  $V_j$  is identified as the numerical solution.

Next, we consider the case of  $E = 8.1 \times 10^{-1}$  MPa. In the range up to approximately  $V_j = 0.6$  m/s, as shown in figure 6 (soft-1),  $H_m/V_j$  is larger than  $\tau_{\text{impact}}$ , and therefore, the integration time window of  $F$  is  $[0, \tau_{\text{impact}}]$ . In this regime, the entire force history is integrated, and thus  $I$  takes the same value as in the case of  $E = 7.0 \times 10^2$  MPa discussed above. However, for  $V_j$  exceeding approximately 0.6 m/s, as shown in figure 6 (soft-2) and (soft-3),  $H_m/V_j$  becomes smaller than  $\tau_{\text{impact}}$ , so that the integration time window of  $F$  is reduced to  $[0, H_m/V_j]$ . Because  $F$  is then only partially integrated, the resulting  $I$  decreases. Moreover, as seen by comparing figure 6 (soft-2) and (soft-3), the integration time window  $[0, H_m/V_j]$  shrinks with increasing  $V_j$ , leading to a reduction in  $I$  as  $V_j$  increases. Figure 6 (soft-2) shows the value of  $I$  at which  $V_j$  becomes the numerical solution for  $E = 8.1 \times 10^{-1}$  MPa. When  $I$ , obtained from the partial integration of  $F$ , equals  $V_j/V_i$ , the corresponding  $V_j$  is identified as the numerical solution.

Finally, by examining the values of  $I$  at which  $V_j$  becomes the numerical solution for each value of  $E$ , as shown in figure 6 (rigid-1), (soft-2) and (soft-4), we find that  $I$  represents either the *total impulse* or a *partial impulse* depending on the relative magnitudes of  $H_m/V_j$

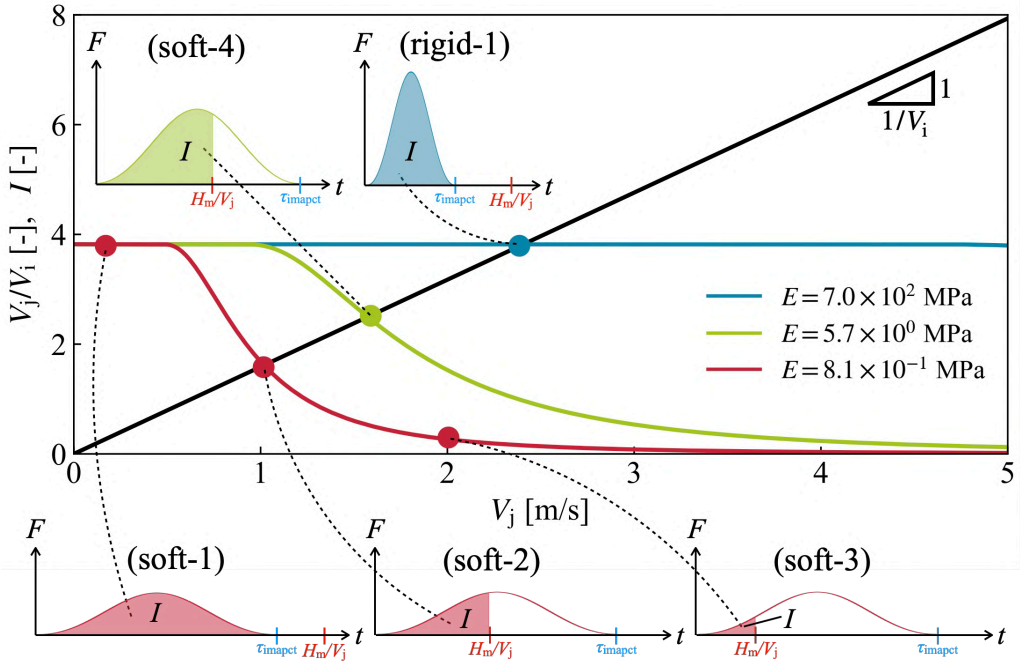


Figure 6. The relationship between an arbitrary  $V_j$ , the left-hand side of the equation (3.11) ( $V_j/V_i$ ), and the right-hand side ( $I$ ). The black line represents  $V_j/V_i$ . The red, green and blue lines indicate  $I$  for  $E = 8.1 \times 10^{-1}$  MPa,  $E = 5.7 \times 10^0$  MPa and  $E = 7.0 \times 10^2$  MPa, respectively. For each value of  $E$ , the numerical solution for  $V_j$  is given by the intersection of the black line with the corresponding coloured line. (rigid-1) denotes the value of  $I$  at the numerical solution for  $V_j$  in the case of  $E = 7.0 \times 10^2$  MPa, which belongs to the *rigid-impact* regime. In this case,  $I$  is obtained by integrating  $F$  over its entire duration. (soft-2) and (soft-4) correspond to the values of  $I$  at the numerical solutions for  $V_j$  when  $E = 8.1 \times 10^{-1}$  MPa and  $E = 5.7 \times 10^0$  MPa, which belongs to the *soft-impact* regime, respectively. Here, the integration window of  $F$  is limited to  $t = H_m/V_j$ , and  $I$  is calculated from a partial integration of  $F$ . (soft-1) to (soft-3) illustrate the relationship between  $V_j$  and  $I$ , together with the integration window, for  $E = 8.1 \times 10^{-1}$  MPa. These results demonstrate that  $I$  represents either the *total impulse* or a *partial impulse* depending on the relative magnitudes of  $H_m/V_j$  and  $\tau_{\text{impact}}$ .

and  $\tau_{\text{impact}}$ . Thus, by treating  $V_j$  as an unknown variable and determining the integration time window such that  $V_j/V_i$  equals  $I$  for each value of  $E$ , the numerical solution of equation (3.11) can be obtained.

### 3.3.4. Mechanism of jet velocity reduction

We validate equation (3.11) by comparing its numerical solutions with the experimental results. The red solid line in figure 3(b) represents the results obtained by numerically solving the equation (3.11) using an explicit Runge–Kutta method combined with trapezoidal integration. Equation (3.11) captures both the small variation of  $V_j/V_i$  in the *rigid-impact* regime and its decrease in the *soft-impact* regime. This shows that  $I$  is well modelled. Here, we discuss the mechanism of the decrease in  $V_j/V_i$  in the *soft-impact* regime by focusing on  $I$ , as calculated from equation (3.11). The shaded regions in figure 5(b) represent  $I$  for each  $E$  obtained from equation (3.11) with  $H = 20$  mm and  $V_i = 0.63$  m/s. In the *rigid-impact* regime ( $E = 1.0 \times 10^3$  MPa to  $2.0 \times 10^5$  MPa), the *total impulse* transferred from the substrate to the container is used to drive the concave gas–liquid interface. In contrast, in the *soft-impact* regime ( $E = 8.1 \times 10^{-1}$  MPa to  $1.9 \times 10^1$  MPa), only the *partial impulse* is used to drive the concave gas–liquid interface compared with the *rigid-impact* regime. In

the *soft-impact* regime, the impact interval becomes longer than the focusing interval, so the effective impulse time window that accelerates the fluid into a jet becomes relatively short. As a result, fluid motion is driven by only the *partial impulse* compared with the *rigid-impact* regime, leading to a decrease in  $V_j/V_i$ . This is the mechanism responsible for the reduction of  $V_j/V_i$  in the *soft-impact* regime.

In this study, we have introduced a new framework in which only the portion of the *total impulse* exerted by the substrate on the container that is actually transmitted to the fluid within the time window effective for jet formation is assumed to drive the jet. This framework enables a unified description of impact-driven jet phenomena across a wide range of substrate stiffness, including both rigid and soft substrates, which have been difficult to treat within conventional pressure–impulse theories.

#### 4. Conclusion

In this study, we have investigated the impact of a fluid-filled container on a soft substrate. The aim of this study was to clarify the mechanism by which the impulse  $I$  used to deform the concave gas–liquid interface is reduced on soft substrates compared with rigid substrates, by focusing on the velocity of the jet generated from the interface after impact.

We conducted drop experiments with a partially liquid-filled test tube while varying the substrate elastic modulus  $E$  over a wide range from  $8.1 \times 10^{-1}$  MPa to  $2.0 \times 10^5$  MPa. We found that the jet velocity  $V_j$  decreases as  $E$  decreases (see figure 2 and figure 3(a)). We also examined the relationship between the impact interval  $\tau_{\text{impact}}$ , defined as the time during which the container and the substrate are in contact, and the focusing interval  $\tau_{\text{focusing}}$ , defined as the time used for a jet to form from a concave gas–liquid interface. Importantly, we found experimentally that the impact interval becomes longer than the focusing interval as  $E$  decreases (see figure 4). This implies that, for smaller values of  $E$ , the jet forms while the container remains in contact with the substrate.

Using dimensional analysis, we examined the relationship between  $V_j$  and  $E$  in detail. We found that the dimensionless jet velocity  $V_j/V_i$  can be organized by the Cauchy number  $\rho_e V_i^2/E$ , which represents the ratio of the inertial force in the container–liquid system to the elastic force of the substrate. When  $V_j/V_i$  is plotted against  $\rho_e V_i^2/E$ , the experimental data collapse onto a single curve (see figure 3(b)). This plot reveals two regimes: one in which  $V_j/V_i$  is nearly constant and another in which  $V_j/V_i$  decreases significantly. The region where  $V_j/V_i$  changes little corresponds to  $\rho_e V_i^2/E < 10^{-4}$ , and this region can be explained using the experimental results of Kiyama *et al.* (2016) obtained with rigid substrates. This indicates that, in the region  $\rho_e V_i^2/E < 10^{-4}$ , the jet velocity can be modelled using the conventional pressure–impulse theory established through impact experiments on rigid substrates (Batchelor 1967; Antkowiak *et al.* 2007; Kiyama *et al.* 2014, 2016). Therefore, we defined the region  $\rho_e V_i^2/E < 10^{-4}$  as the *rigid-impact* regime. In contrast, the region where  $V_j/V_i$  decreases significantly corresponds to  $\rho_e V_i^2/E > 10^{-4}$ . In this region, the jet velocity cannot be modelled using conventional pressure–impulse theory. We experimentally showed for the first time that the effect of soft substrates becomes significant in fluid motion when  $\rho_e V_i^2/E > 10^{-4}$ . Therefore, we defined the region  $\rho_e V_i^2/E > 10^{-4}$  as the *soft-impact* regime and discussed the mechanism of jet velocity reduction in this regime.

The key observation for elucidating the mechanism underlying the reduction of  $V_j/V_i$  is the relative ordering of two timescales: the impact interval  $\tau_{\text{impact}}$  and the focusing interval  $\tau_{\text{focusing}}$ . In the *rigid-impact* regime,  $\tau_{\text{impact}} < \tau_{\text{focusing}}$  holds (see figure 4(a)). In this case, the contact force acts only over a short time, and the fluid subsequently focuses after the

contact has ended. In this limit, it is natural to relate jet formation to the *total impulse* delivered during contact. In contrast, in the *soft-impact* regime, we find  $\tau_{\text{impact}} > \tau_{\text{focusing}}$ , indicating that jet formation starts while contact is still ongoing (see figures 4(b,c)). In this case, the jet cannot be driven by the *total impulse* transmitted over the entire contact duration, because the jet forms before the *total impulse* has been delivered to the fluid. This observation motivates a framework in which the jet is governed by the impulse accumulated up to the jet-formation time, i.e., the *partial impulse* (see figure 5(b) and figures 6 (soft-2)–(soft-4)).

This framework can be expressed by integrating the contact force over a finite time window. Importantly, the present formulation automatically recovers the *rigid-impact* limit. When  $\tau_{\text{impact}} < \tau_{\text{focusing}}$ , the contact force vanishes for  $t > \tau_{\text{impact}}$ , and therefore, integrating up to  $t = \tau_{\text{focusing}}$  is equivalent to integrating over the entire contact duration. In contrast, when  $\tau_{\text{impact}} > \tau_{\text{focusing}}$ , the upper limit  $t = \tau_{\text{focusing}}$  truncates the force history, so that only a portion of the *total impulse* contributes to jet formation. In this paper, we formulated this framework as a predictive model by combining momentum conservation with a contact force model based on the elastic foundation model. As a result, the impulse  $I$  was formulated as shown in equations (3.11) and (3.12). By comparing the experimental results with numerical solutions of the model equation, treating  $V_j$  as an unknown, we demonstrated that the model quantitatively accounts for the experimental observations (see figure 3(b)).

The key contribution of this study is the introduction of a framework in which only the portion of the *total impulse* transmitted from the substrate to the container that is actually delivered to the fluid within the effective time window for jet formation drives the jet. This framework enables a unified description of impact-driven jetting over a wide range of substrate stiffness, including both rigid and soft substrates. In particular, for sufficiently soft substrates, the contact duration between the substrate and the container becomes longer than the time required for jet formation, so that the effective time window during which the fluid is accelerated into a jet becomes relatively short. As a result, in the case of soft substrates, the fluid motion is driven by only a *partial impulse* compared with that for rigid substrates, leading to a reduction in the jet velocity.

## Appendix A. Method for measuring the substrate elastic modulus

In this study, the elastic modulus  $E$  of rubber and elastomer substrates was measured experimentally. In this section, we describe the method used to measure  $E$ . The substrate elasticity can be estimated from the surface deformation  $\delta$  when a rigid sphere is pressed vertically onto the substrate with a load  $P$  (see figure 7(a)). In the experiment, the substrate elastic modulus was calculated using the elastic foundation model (Johnson 1987) as

$$E = \frac{Ph}{\pi R_s \delta^2}. \quad (\text{A } 1)$$

Here,  $h$  denotes the substrate thickness, and  $R_s$  is the radius of the rigid sphere. In this experiment, a steel sphere with a diameter of  $2R_s = 12.7$  mm was used.

Next, the experimental procedure is described. As shown in figure 7(b), a metal rod was fixed with screws to a micrometre (Newport, M-562 Series) that can move vertically. The steel sphere was fixed to a metal rod using adhesive. An electronic balance (AS ONE Corporation, AXA20002) was placed beneath the steel sphere, and an aluminium plate and the substrate to be measured were placed on the balance. The balance was zeroed with the aluminium plate and the substrate on it. By moving the micrometre, the steel sphere moved vertically together with the micrometre (see figure 7(b)). The micrometre was adjusted so that the distance between the steel sphere and the substrate was zero ( $\delta = 0$ ). At this position, the reading of the balance was zero. From this state, the micrometre was moved downward by a displacement  $\delta$ , causing the steel sphere to move downward by  $\delta$  and deform the substrate surface by  $\delta$  (see figure 7(a)). The applied load  $P$  on the substrate (see figure 7(a)) was calculated as  $P = mg$ , where  $m$  is the apparent mass measured by the balance and  $g = 9.81 \text{ m/s}^2$ .  $\delta$  ranged from  $10 \mu\text{m}$  to  $430 \mu\text{m}$  in steps of  $10 \mu\text{m}$ , and the corresponding  $P$  was recorded for each  $\delta$ . The substrate

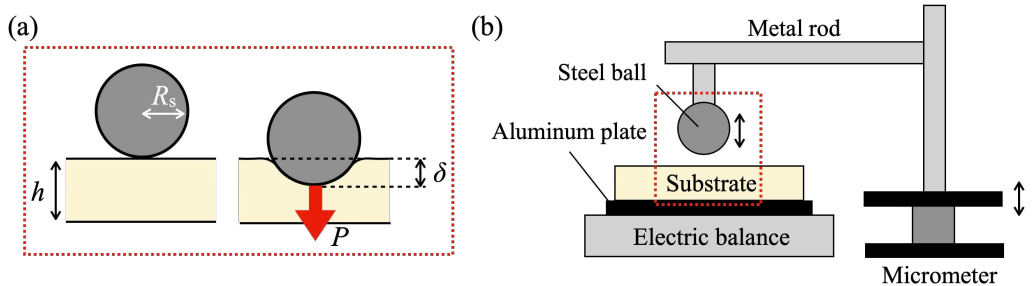


Figure 7. (a) When  $\delta$  is applied to the substrate surface,  $P$  acts on the substrate.  $h$  is the substrate thickness, and  $R_s$  is the radius of the iron ball. (b) A schematic of the experimental setup for measuring substrate elastic modulus.

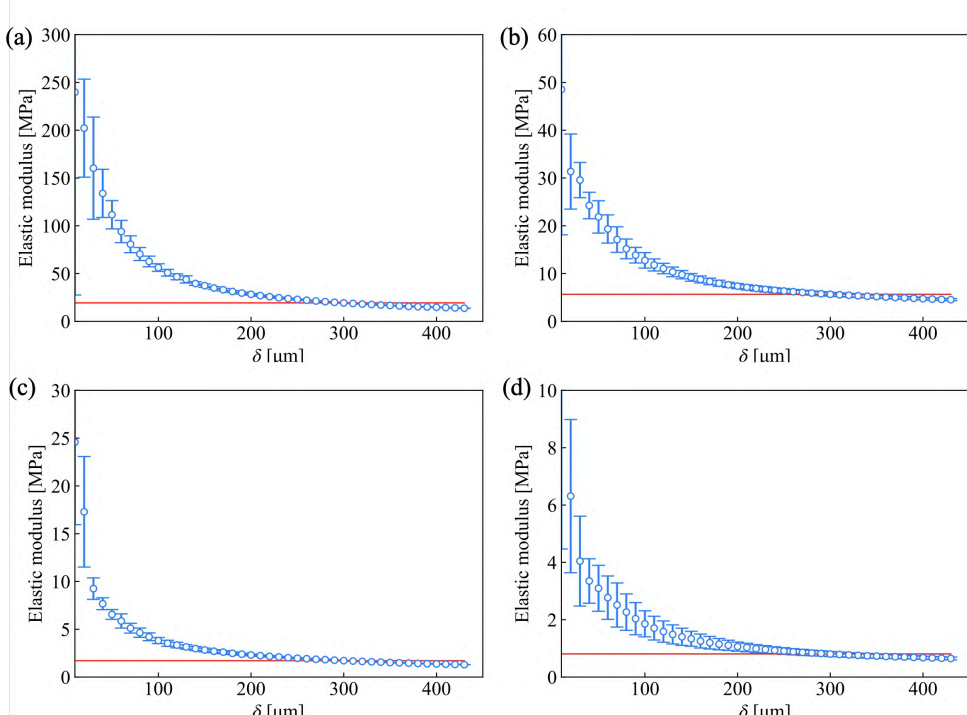


Figure 8. The relationship between the elastic modulus calculated from equation (A 1) and  $\delta$  for (a) rubber, (b) PDMS10, (c) PDMS20, and (d) PDMS30. The red solid line represents the average elastic modulus for cases with  $\delta \geq 200 \mu\text{m}$  corresponding to  $E$ .

elastic modulus at each  $\delta$  was then calculated using equation (A 1). Each measurement was repeated five times for each value of  $\delta$ .

Figure 8 shows the relationship between the elastic modulus calculated from equation (A 1) and  $\delta$  for rubber and elastomer substrates. Panels (a)–(d) correspond to rubber, PDMS10, PDMS20 and PDMS30, respectively. The plotted values are the averages of five measurements, and the error bars represent the standard deviation. The elastic modulus converges as  $\delta$  increases. In this study, the elastic modulus averaged over  $\delta \geq 200 \mu\text{m}$  was adopted as the representative value  $E$  for each substrate (the red lines in figure 8 indicate the averaged value of the elastic modulus for  $\delta \geq 200 \mu\text{m}$  corresponding to  $E$ ). Using this method, the values of  $E$  for the rubber and elastomer substrates are summarized in table 1.

## Appendix B. Fabrication procedure of the substrate using polydimethylsiloxane (PDMS)

In the experiment, polydimethylsiloxane (PDMS) elastomer substrates were prepared. In this section, the fabrication procedure for the PDMS substrates is described. First, the base material (DOW, SILPOT 184 Silicone Elastomer Base) and the curing agent (DOW, SILPOT 184 Silicone Elastomer Curing Agent) were thoroughly mixed at mass ratios of 10:1, 20:1 and 30:1. Next, the mixed PDMS was degassed in a vacuum chamber for one hour. The degassed PDMS was then poured into a container (100 × 100 × 25 mm) fabricated using a 3D printer (Bambu Lab A1 3D Printer) and degassed again for one hour. During this process, care was taken to keep the container level to ensure a uniform substrate thickness. The substrate was then heated at 80°C for two hours using a heater (Formlabs, Formlabs Form Cure L). After heating and confirming that the PDMS was fully cured, the PDMS substrate was removed from the container. Finally, baby powder (SiCCAROL-Hi, Asahi Group Foods Co., Ltd.) was applied to the PDMS substrate surface to remove surface tackiness.

## Appendix C. Validation of the elastic foundation model

In §3.3, a new model for the jet velocity was developed by modelling the impulse used to drive the concave gas–liquid interface based on the elastic foundation model. In this section, the validity of the elastic foundation model is assessed by comparing the experimentally measured contact force with that calculated using the Hertz model.

### C.1. Measurement of the contact force using an accelerometer

In this section, the method used to measure the contact force is described. The experimental setup was based on the method proposed by Kurihara *et al.* (2025), and is shown in figure ???. An accelerometer (Showa Sokki Co., Ltd., MODEL 2350, sensitivity 0.347 pC/(m/s<sup>2</sup>)) was firmly fixed to an aluminium plate using screws, and the aluminium plate was then bonded to the top of the test tube. A steel S-shaped hook with a jig was attached to the top of the accelerometer using double-sided tape, and the impactor was placed above the substrate using an electromagnet. The accelerometer output an electric charge proportional to the applied acceleration. The accelerometer was connected to a charge amplifier (Showa Sokki Co., Ltd., MODEL 4035-50) to convert the charge signal into a voltage signal. The charge amplifier was connected to an oscilloscope (Iwasaki Communication Co., Ltd., DS-5554A), and the voltage time history was recorded. The experimental conditions were the same as those described in §2.

The raw voltage data recorded by the oscilloscope contained significant high-frequency noise, which was removed using a fast Fourier transform. The filtered voltage signal [V] was then converted into acceleration  $a$  [m/s<sup>2</sup>] using the acceleration scale set in the charge amplifier. The acceleration was further converted into force  $F$  [N] using the equation of motion,  $F = ma$ . In this experiment,  $F$  was calculated by multiplying  $a$  by the mass  $m$  of the impactor.

The black solid lines in figure 10 show the time histories of  $F$  measured using the accelerometer ( $H = 20$  mm and  $V_i = 0.63$  m/s). Panels (a)–(d) correspond to  $E = 2.0 \times 10^5$  MPa,  $E = 1.9 \times 10^3$  MPa,  $E = 5.7 \times 10^0$  MPa and  $E = 8.1 \times 10^{-1}$  MPa, respectively. In panels (b)–(d),  $F$  rises rapidly, reaches a peak, and then decreases. In contrast, panel (a) shows two peak values. The second peak is likely caused by the accelerometer detecting pressure fluctuations in the liquid (Kurihara *et al.* 2025).

### C.2. Comparison between the experimental contact force and impact models

In §3.3, the impact of an object with a hemispherical bottom onto the substrate was modelled as the impact of a rigid sphere. In §3.3, the elastic foundation model was used to model the contact force. However, the Hertz model is another representative model for the impact of a rigid sphere onto a substrate. In this section, the differences between the elastic foundation model and the Hertz model are discussed. In addition, the contact force measured with the accelerometer is compared with predictions from the elastic foundation and Hertz models to assess the validity of using the elastic foundation model.

The main difference between the elastic foundation model and the Hertz model lies in the potential of the contact displacement. Figure 11 shows the displacement potentials for the two impact models. The Hertz model assumes contact between a rigid sphere and a substrate with infinite thickness, and also assumes that the surface deformation of the substrate is very small (Johnson 1987). In this case, the contact displacement follows a spherical potential (see figure 11). Therefore, the Hertz model is suitable for modelling impacts between stiff substrates and rigid spheres. However, the Hertz model cannot fully capture real behaviour when the substrate is thin or when the surface deformation is large compared to the substrate thickness. In contrast, the elastic foundation model assumes contact between a rigid sphere and a substrate with finite thickness (Johnson 1987), for which the contact displacement follows a vertical potential (see figure 11). Therefore, the elastic foundation model is effective for modelling impacts in cases where the effect of substrate thickness cannot be neglected.

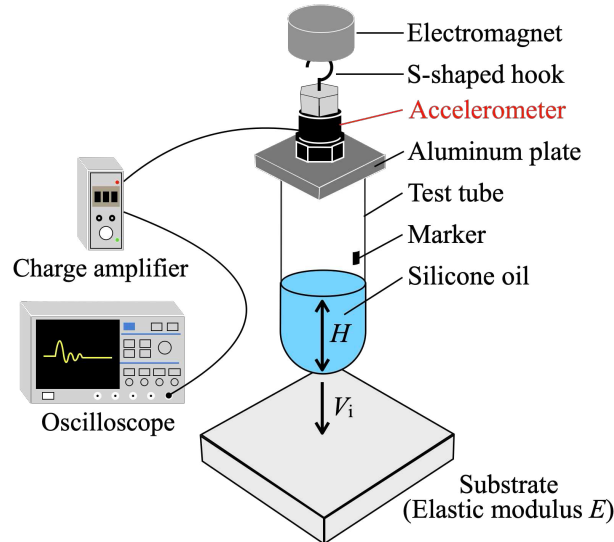


Figure 9. A schematic of the experimental setup for measuring the contact force using an accelerometer.

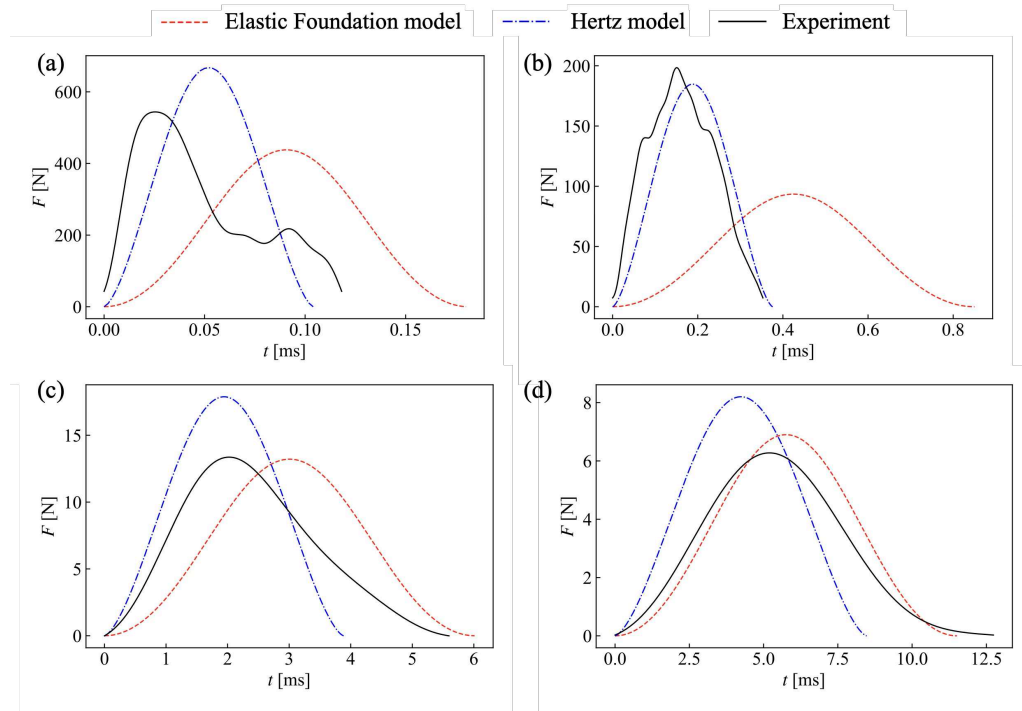


Figure 10. A comparison of the experimental force  $F$  with the Hertz model and the elastic foundation model. Panels (a)–(d) correspond to  $E = 2.0 \times 10^5$  MPa,  $E = 1.9 \times 10^3$  MPa,  $E = 5.7 \times 10^0$  MPa, and  $E = 8.1 \times 10^{-1}$  MPa, respectively. The conditions are  $H = 20$  mm and  $V_i = 0.63$  m/s.

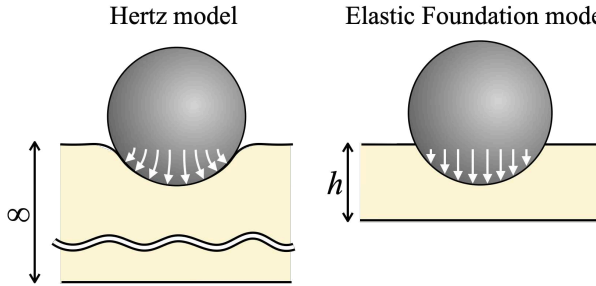


Figure 11. A comparison of contact-displacement potentials between the Hertz model and the elastic foundation model.

In the Hertz model,  $F$  is expressed in terms of the effective elastic modulus  $E^*$ , the radius of the rigid sphere  $R$  and the surface displacement of the substrate  $z$ , as

$$F = \frac{4}{3} E^* R^{1/2} z^{3/2}. \quad (\text{C } 1)$$

$E^*$  is given in terms of the elastic modulus  $E_1$  and  $E_2$  and the Poisson's ratios  $\nu_1$  and  $\nu_2$  of the rigid sphere and the substrate, respectively, as

$$E^* = \left( \frac{1 - \nu_1^2}{E_1} + \frac{1 - \nu_2^2}{E_2} \right)^{-1}. \quad (\text{C } 2)$$

To calculate the contact force acting on the container in this experiment using the Hertz model, the container can be treated as a rigid sphere with a hemispherical bottom. Specifically, the contact force predicted by the Hertz model can be obtained by numerically calculating equation (3.8), substituting in equations (C 1) and (C 2).

Next, the contact force measured in the experiment is compared with the predictions of the elastic foundation model and the Hertz model. Figure 10 shows a comparison for  $F$ . The red dashed lines represent the elastic foundation model, and the blue dashed lines represent the Hertz model. Here, we focus mainly on the end time of the  $F$ , which corresponds to the moment when the container separates from the substrate, when comparing the two models with the experimental data. In the *rigid-impact* regime shown in figures 10(a, b), the force profile predicted by the Hertz model captures the experimental trend better. In contrast, in the *soft-impact* regime shown in figures 10(c, d), the elastic foundation model reproduces the experimental trend more accurately. These results indicate that the impact model that best describes the experimental force profile depends on  $E$ .

Based on this observation, we consider which impact model is appropriate for the present study. We argue that, for the *soft-impact* regime, the impact interval becomes longer than the focusing interval, resulting in a relatively shorter effective impulse time window that accelerates the fluid into a jet. From this perspective, the most appropriate impact model is the one that accurately captures the end time of  $F$  at small  $E$ . Therefore, the elastic foundation model is adopted in this study.

**Acknowledgments** This work was funded by the Japan Society for the Promotion of Science (Grant Nos. 20H00222, 20H00223, 20K20972, and 24H00289) and the Japan Science and Technology Agency (Grant Nos. PRESTO JPMJPR21O5 and SBIR JPMJST2355).

**Declaration of Interests** The authors report no conflict of interest.

#### REFERENCES

- ANDRADE, K., CATALÁN, J., MARÍN, J. F., SALINAS, V., CASTILLO, G., GORDILLO, L. & GUTIÉRREZ, P. 2023 Swirling Fluid Reduces the Bounce of Partially Filled Containers. *Phys. Rev. Lett.* **130** (24), 244001.
- ANTKOWIAK, A., BREMOND, N., DIZÈS, S. LE & VILLERMAUX, E. 2007 Short-term dynamics of a density interface following an impact. *J. Fluid. Mech.* **577**, 241–250.
- ASHBY, M. F. & JONES, D. R. 2012 *Engineering Materials 1: An Introduction to Properties, Applications and Design*. Elsevier.
- BATCHELOR, G. K. 1967 *An Introduction to Fluid Dynamics*. Cambridge University Press.
- BOCQUET, L. 2003 The physics of stone skipping. *Am. J. Phys.* **71** (2), 150–155.
- CHENG, X., CHEN, X., DING, H., ZHANG, C. Y., HU, H. & JIA, L. 2024 Viscous influences on impulsively generated focused jets. *Phys. Rev. Fluids* **9** (8), L082001.
- COOKER, M. J. & PEREGRINE, D. H. 1995 Pressure-impulse theory for liquid impact problems. *J. Fluid Mech.* **297**, 193–214.
- DIAS, F. & GHIDAGLIA, J. M. 2018 Slamming: Recent Progress in the Evaluation of Impact Pressures. *Annu. Rev. Fluid Mech.* **50** (1), 243–273.
- GLASHEEN, J. W. & McMAHON, T. A. 1996a A hydrodynamic model of locomotion in the Basilisk Lizard. *Nature* **380** (6572), 340–342.
- GLASHEEN, J. W. & McMAHON, T. A. 1996b Vertical water entry of disks at low Froude numbers. *Phys. Fluids* **8** (8), 2078–2083.
- GRUMSTRUP, T., KELLER, J. B. & BELMONTE, A. 2007 Cavity ripples observed during the impact of solid objects into liquids. *Phys. Rev. Lett.* **99** (11), 114502.
- HSIEH, S.T. & LAUDER, G.V. 2004 Running on water: Three-dimensional force generation by basilisk lizards. *PNAS* **101** (48), 16784–16788.
- HU, Z. & LI, Y. P. 2025 Breaking wave impacts on an elastic plate. *J. Fluid Mech.* **1015**, A54.
- JOHNSON, K. L. 1987 *Contact Mechanics*. Cambridge University Press.
- JOSSERAND, C., RAY, P. & ZALESKI, S. 2016 Droplet impact on a thin liquid film: Anatomy of the splash. *J. Fluid Mech.* **802**, 775–805.
- JOSSERAND, C. & THORODDSEN, S.T. 2016 Drop impact on a solid surface. *Annu. Rev. Fluid Mech.* **48** (1), 365–391.
- KAMAMOTO, K., ONUKI, H. & TAGAWA, Y. 2021 Drop-on-demand painting of highly viscous liquids. *Flow* **1**, E6.
- KAPSENBERG, G. K. 2011 Slamming of ships: Where are we now? *Phil. Trans. R. Soc. A.* **369** (1947), 2892–2919.
- KIYAMA, A., NOGUCHI, Y. & TAGAWA, Y. 2014 The generation of a liquid jet induced by a pressure impulse (experimental study on the jet velocity). *Trans. JSME (Japan.)* **80** (814), FE0151–FE0151.
- KIYAMA, A., TAGAWA, Y., ANDO, K. & KAMEDA, M. 2016 Effects of a water hammer and cavitation on jet formation in a test tube. *J. Fluid Mech.* **787**, 224–236.
- KOBAYASHI, K., WATANABE, H., YEE, J., TORII, S., KURITA, M. & TAGAWA, Y. 2024 Development and evaluation of on-demand printing technology for highly viscous liquids. *J. Imaging Soc. Jpn. (Japan.)* **63** (5), 014035.
- KRISHNAN, S., BHARADWAJ, S. V. & VASAN, V. 2022 Impact of freely falling liquid containers and subsequent jetting. *Exp Fluids* **63** (7), 108.
- KURIHARA, C., KIYAMA, A. & TAGAWA, Y. 2025 Pressure fluctuations of liquids under short-time acceleration. *J. Fluid Mech.* **1003**, 224–236.
- LAVRENTIEV, M. & CHABAT, B. 1980 *Effets Hydrodynamiques Et Modèles Mathématiques*. Éditions MIR.
- MARUOKA, H. 2023 A framework for crossover of scaling law as a self-similar solution: Dynamical impact of viscoelastic board. *Eur. Phys. J. E* **46** (5), 35.
- MICHELE, S. & SAMMARCO, P. 2025 Weakly nonlinear theory of water hammer induced by slow valve manoeuvres. *J. Fluid Mech.* **1021**, A36.
- MILGRAM, J. H. 1969 The motion of a fluid in a cylindrical container with a free surface following vertical impact. *J. Fluid Mech.* **37** (3), 435–448.
- ONUKI, H., OI, Y. & TAGAWA, Y. 2018 Microjet Generator for Highly Viscous Fluids. *Phys. Rev. Applied* **9** (1), 014035.
- PAN, Z., KIYAMA, A., TAGAWA, Y., DAILY, D. J., THOMSON, S. L., HURD, R. & TRUSCOTT, T. T. 2017 Cavitation onset caused by acceleration. *Proceedings of the National Academy of Sciences* **114** (32), 8470–8474.

## Interfacial dynamics induced by impacts across rigid and soft substrates

- PEREGRINE, D. H. 2003 Water-wave impact on walls. *Annu. Rev. Fluid Mech.* **35**, 23–43.
- PETERS, I. R., TAGAWA, Y., OUDALOV, N., SUN, C., PROSPERETTI, A., LOHSE, D. & VAN DER MEER, D. 2013 Highly focused supersonic microjets: numerical simulations. *J. Fluid Mech.* **719**, 587–605.
- PHILIPPI, J., ANTKOWIAK, A. & LAGRÉE, P. Y. 2018 A pressure impulse theory for hemispherical liquid impact problems. *Eur. J. Mech. B. Fluids* **67**, 417–426.
- PHILIPPI, J., LAGRÉE, P. Y. & ANTKOWIAK, A. 2016 Drop impact on a solid surface: Short-time self-similarity. *J. Fluid Mech.* **795**, 96–135.
- RABBI, R., C., MORTENSEN, KIYAMA, A. & TRUSCOTT, T. 2024 Altered deep-seal water entry behavior of a sphere by a neighboring sphere and/or solid boundary. *Ocean Eng.* **313**, 119377.
- ROSELLINI, L., F., HERSEN, CLANET, C. & BOCQUET, L. 2005 Skipping stones. *J. Fluid Mech.* **543**, 137–146.
- SHUKLA, V. C., HIGUITA-CASTRO, N., NANA-SINKAM, P. & GHADIALI, S. N. 2016 Substrate stiffness modulates lung cancer cell migration but not epithelial to mesenchymal transition. *J. Biomed. Mater. Res. Part A* **104** (5), 1182–1193.
- TAGAWA, Y., OUDALOV, N., VISSER, C. W., PETERS, I. R., VAN DER MEER, D., SUN, C., PROSPERETTI, A. & LOHSE, D. 2012 Highly focused supersonic microjets. *Phys. Rev. X* **2** (3), 031002.
- THORODDSEN, S. T., ETOH, T. G., TAKEHARA, K. & TAKANO, Y. 2004 Impact jetting by a solid sphere. *J. Fluid Mech.* **499**, 139–148.
- TRUSCOTT, T. T., EPPS, B. P. & BELDEN, J. 2014 Water entry of projectiles. *Annu. Rev. Fluid Mech.* **46** (1), 355–378.
- TSAI, H. W., TSAI, H. C., WU, W. F. & LAI, C. L. 2022 Experimental results and mathematical formulation of non-spinning stone-skipping process. *Sci Rep* **12** (1), 16372.
- WATANABE, H., KUSUNO, H. & TAGAWA, Y. 2025 Effect of a converging container shape on the velocity of an impact-induced focused liquid jet. *Int. J. Multiphase Flow* **193**, 105348.
- XIE, W. 2025 Preliminary semi-analytical investigation of momentum exchange in a bouncing container filled with swirling fluid: Pressure impulse induced by central jet. *Mech. Res. Commun.* **144**, 104380.
- YAHAMED, A., IKONOMOV, P., FLEMING, P. D., PEKAROVICOVA, A., GUSTAFSON, P., ALDEN, A. Q. & ALFRAFEEK, S. 2016 Mechanical properties of 3D printed polymers. *J. Print Media Technol. Res.* **5** (4), 273–289.
- YOKOYAMA, Y., ICHIHARA, S. & TAGAWA, Y. 2024 High-speed photoelastic tomography for axisymmetric stress fields in a soft material: Temporal evolution of all stress components. *Opt. Lasers Eng.* **178**, 108224.
- ZHANG, Y., GUO, T., VLACHOS, P. & ARDEKANI, A. M. 2020 Velocity scaling and breakup criteria for jets formed due to acceleration and deceleration process. *Phys. Rev. Fluids* **5** (7), 074003.